Continuous Hydrothermal Synthesis of Metal Germanates (M_2GeO_4; M = Co, Mn, Zn) for High Capacity Negative Electrodes in Li-ion Batteries

Dustin Bauer,[1,2] Thomas E Ashton,[1] Alexandra R. Groves,[1,3] Avishek Dey,[4] Satheesh Krishnamurthy,[4] Noriyoshi Matsumi,[2] and Jawwad A. Darr[1]*

[1] Department of Chemistry, University College London, 20 Gordon Street, London, WC1H 0AJ, UK
[2] School of Materials Science, Japan Advanced Institute of Science and Technology, 1-1 Asahidai, Nomi, Ishikawa, Japan
[3] Research Complex at Harwell, Rutherford Appleton Laboratory, Harwell, Didcot OX11 0FA, UK
[4] School of Engineering and Innovation, The Open University, Milton Keynes MK7 6AA, UK

*Corresponding author: Professor Jawwad A. Darr

Office telephone: +44 (0)20 7679 4345

Research webpages http://www.ucl.me.uk

Abstract

Nanosized metal germanates (M_2GeO_4; M = Co, Mn, Zn) were synthesised using a continuous hydrothermal flow synthesis process for the first time. Phase-pure rhombohedral Zn_2GeO_4 nanorods, cubic spinel Co_2GeO_4 nanoparticles, and orthorhombic Mn_2GeO_4 nanotubes/nanoparticles were obtained. The electrochemical properties of all samples as active materials for negative electrodes in Li-ion half cells was explored. The galvanostatic and potentiodynamic testing was conducted in the potential range 3.00 to 0.05 V vs. Li/Li^+. The results suggest that both alloying and conversion reactions associated with Ge contributed to the stored charge capacity; Zn_2GeO_4 showed a high specific capacity of 600 mAh g^{-1} (10 cycles at 0.1 A g^{-1}) due to alloying and conversion reactions for both Ge and Zn. Mn_2GeO_4 was studied for the first time as a potential negative electrode material in a Li-ion half-cell; an excellent specific charge capacity of 510 mAh g^{-1} (10 cycles / 0.1 A g^{-1}) was obtained with a significant contribution to charge arising from the conversion reaction of Mn to MnO upon delithiation. In contrast, Co_2GeO_4 only showed a specific capacity of 240 mAh g^{-1}, after 10 cycles at the same current rate, which suggested that cobalt had little or no benefit for enhancing stored charge in the germanate.

Keywords: Alloying material, ternary oxide, germanate, negative electrode

Introduction

Growing awareness of anthropomorphic climate change due to greenhouse gases has made research of secondary Li-ion battery (LIB) increasingly relevant.[1] The major advantage of LIBs over other electrochemical energy storage technologies is their superior energy densities.[2] Whilst most commercial LIBs employ graphite as active material in the negative electrode, many other active materials have been proposed to improve upon some of the detrimental properties of graphite; safety concerns because of potential cell failure due to lithium dendrite formation,[3] irreversible capacity losses during the first cycle,[3,4] and poor rate performance.[4]

Lithium insertion materials including some transition metal oxides, have been studied as active materials with superior rate performance.[5] When specific capacity is the major focus, alloying materials such as Si, Sn, and ternary oxides are generally considered.[6,7] Graphite has a theoretical capacity of 372 mAh g^{-1} (1 Li^+ per six C), whereas alloying materials have theoretical capacities of up to 3572 mAh g^{-1} (for silicon, 15 Li^+ per Si).[7,8] The major disadvantages of alloying active materials, however, have been reported to be poor rate performance due to the diffusion-limited nature of the alloying process and large capacity fading due to the substantial volume changes upon lithiation/delithiation.[6,9,10] However, it has previously been reported that morphology can significantly influence the cycling performance of alloying Li-ion battery active materials,[11] and that nanostructure[12] and core-shell designs[13] can improve electrochemical cycling stability.

Transition metal oxides such as manganese oxides, iron oxides, cobalt oxides, and nickel oxides are known to undergo conversion reactions upon lithiation. The metals are reduced to an oxidation state of 0, whereas the oxygen forms lithium superoxide (Li_2O) with lithium ions.[12] Although these materials can show high reversible specific capacities, they typically suffer from large voltage hysteresis,[14] low energy efficiencies,[15] large capacity fading,

and poor rate performance.[2] Ternary mixed-metal oxides such as ferrites, cobaltites, and germanates have been suggested as possible alternatives to Si or Sn because of high ionic transport coefficients, high electronic conductivity, and relatively simple synthesis methods.[12]

Elemental Ge has received interest as a potential alloying active material for LIB negative electrodes because of its relatively high theoretical capacity (1384 mAh g^{-1}),[16] the significantly higher diffusivity of Li^+ in Ge compared to the more commonly studied Si (up to 400 times higher at room temperature),[17] as well as its significantly higher electronic conductivity compared to Si (up to 10 000 times higher at room temperature).[18] However, Ge suffers from large volume changes upon lithiation (260 %),[19] which occurs according to Equation 1:[20]

$$Ge + 4.4Li \leftrightarrow Li_{4.4}Ge \quad \text{(Eq. 1)}$$

Because Ge is expensive compared to some other transition metal oxides, GeO_2 (germania) has been considered because of the its lower cost. Upon the first lithiation, germania is irreversibly reduced to elemental Ge as shown in equation 2:[16]

$$GeO_2 + 4Li \rightarrow Ge + 2Li_2O \quad \text{(Eq. 2)}$$

Upon further lithiation, reversible alloying of Ge with Li occurs according to Eq. 1. Whilst Eq. 1 and Eq. 2 give theoretical reversible gravimetric and volumetric capacities of 1100 mAh g^{-1} and 4 653 mAh cm^{-3}, respectively (much higher than those for graphite),[16] however, capacity retention in germania has been reported to be inadequate.[21]

To overcome both the poor cyclability and high cost of Ge and GeO_2, metal germanates M_2GeO_4 (M = e.g. Zn, Co, Fe, etc.) have been studied as active negative electrode materials. Zn_2GeO_4 is of interest because of the high theoretical capacity of 1443 mAh g^{-1}, which is a result of the electrochemical activity of both Zn and Ge species via alloying (as the metal) or conversion reactions (as the oxides).[22,23] Co_2GeO_4 has been studied because of the

complementary conversion reaction of Co with Li_2O, which can occur at higher potentials vs. Li/Li^+ than the alloying/dealloying reaction of Ge, which results in a highly conductive amorphous network of Co and Li_2O to improve the Ge alloying reaction.[20] Mn-doping of Zn_2GeO_4 has been reported in the literature and was shown to improve the specific capacity at all applied specific currents compared to Zn_2GeO_4.[24] Morphology has also been shown to significantly influence performance, with hollow nanoparticles significantly outperforming short nanorods of Zn_2GeO_4.[11]

Whilst nanosizing the morphology of M_2GeO_4 active materials has been reported to improve cycling stability, rate performance, and increase overall capacity, nanosizing often requires long synthesis steps (> 10 hours),[11,23–26] multiple steps,[23,25] and is therefore limited in the potential for scalability.[20,22,27] Herein, we describe a single step continuous hydrothermal flow synthesis (CHFS) process for the production of three different metal germanates (Zn_2GeO_4, Co_2GeO_4, Mn_2GeO_4) with different crystal structures. The CHFS methodology was recently reviewed in by the authors and has shown to be a powerful tool in the continuous preparation of oxide, sulphide, metal nanoparticles for use in Na-ion batteries, Zn-air batteries, fuel cells, photocatalysts, transparent conducting oxides, optical modifiers, pigments, antibacterials and magnetic materials among other applications.[29]

Materials & Methods

Chemicals

The chemicals used were of analytical grade and used without purification. The chemicals were purchased from Sigma-Aldrich, Dorset, UK, unless stated otherwise. The chemicals included GeO_2 (> 99.99 %,), KOH (analytical reagent grade, Fisher Chemicals, Loughborough, UK), $Zn(C_2H_3O_2)_2{\cdot}2H_2O$ (zinc acetate dihydrate, analytical grade), $Co(C_2H_3O_2)_2{\cdot}4H_2O$ (cobalt

acetate tetrahydrate, reagent grade), $Mn(C_2H_3O_2)_2{\cdot}4H_2O$ (manganese acetate tetrahydrate, > 99 %), Super P conductive carbon (Alfa Aesar, Heysham, UK), polyvinylidene fluoride (PVDF, PI-KEM, Staffordshire, UK), and N-methyl-2-pyrrolidone (NMP).

Continuous hydrothermal flow synthesis

A continuous hydrothermal flow synthesis (CHFS) process was used to synthesise nanoparticles of Zn_2GeO_4, Co_2GeO_4, and Mn_2GeO_4. This CHFS process has previously been described by some of the authors at both pilot scale[28] and at lab scale.[29–32] The process used herein was at the lab scale, a diagram of which can be found in the Supplementary information (see Figure S1). Herein, a water feed above the critical temperature and pressure of water (T_c = 374 °C; p_c = 22.1 MPa) was mixed with an ambient temperature flow of aqueous metal salts. This flow of aqueous metal salts consisted of a flow of metal precursors for the metal germanates (consisting of the premade solution containing the Ge precursor and one of the Zn, Co, or Mn aqueous salts), which was pre-mixed with a flow of base (KOH_{aq}). The following concentrations were used as feeds; the KOH concentration was 0.5 M, whilst for the metal feed, the [Ge] was always 0.04 M, and the [M] was 0.08 M (where M is either Co, Zn or Mn). The supercritical water feed and the ambient temperature aqueous metal salt flow were combined in a co-current, patented Confined Jet Mixer (CJM), which was made from off the shelf Swagelok™ parts.[33] The temperature at the mixing point in the CJM was 335 °C as a result of balanced flows from Pump 1 (80 mL min^{-1}, supercritical water) and Pumps 2 and 3 (40 mL min^{-1} each, aqueous metal precursors and KOH feeds, respectively). After mixing in the CJM and a 5 seconds residence time, the newly formed particle slurry was cooled to ca. 40 °C in a pipe-in-pipe heat exchanger.[34] The nanoparticle slurry was collected from the outlet of the back-pressure regulator and then cleaned by dialysis using DI water for 48 hours by which time the conductivity of the water was less than 50 µS cm^{-1}. Then, the samples were concentrated into a sludge that was freeze-dried via cooling to below −40 °C in a vacuum of 13.3 Pa using

a Virtis Genesis 35XL freeze-drier (SP Scientific, Pennsylvania, US). The freeze-dried powders were used as active materials without any heat-treatment or further processing. The rate of synthesis was ca. 25 g h^{-1} for each sample.

Physical characterisation

Powder X-ray diffraction (PXRD) of all three powders was carried out in the 2θ range 7.5 to 30.0°, using Mo-Kα radiation (λ = 0.7107 Å). The step time was set to 20 s and the step size to 0.5° 2θ. The PXRD patterns were collected on a STOE StadiP diffractometer.

High-resolution Transmission electron microscopy (TEM) and energy dispersive X-ray spectroscopy (EDX) were performed using a JOEL JEM 2100 with a LaB_6 filament for size and particle morphology analysis as well as elemental analysis and mapping, respectively. The samples were dispersing in methanol and pipetted onto a 300-mesh copper grid (Agar Scientific, Stansted, UK). A Gatan Orius digital camera was used for the image capture of the TEM micrographs.

X-ray photoelectron spectroscopy (XPS) used a Thermo Scientific K-alpha™ spectrometer (Al-Kα radiation) with a 128-channel position sensitive detector to analyse the valence states and concentrations of metal ions on the nanoparticle surfaces. For Ge, Zn, Mn, Co, and O, high-resolution regional scans were conducted at 50 eV. CasaXPS™ software (version 2.3.19) was used to process the data.

The Brunauer-Emmett-Teller (BET) technique was used to determine the specific surface areas of the powders. BET measurements used a Micrometrics Tristar II. Before BET measurements, the samples were degassed at 120 °C for 12 h.

Electrochemical characterisation

Anodes for LIBs were prepared by mixing the corresponding metal germanate active material powder with Super P conductive carbon and PVDF binder in the wt% ratio of 80:10:10. The

PVDF was added in the form of a pre-dissolved 5 wt% solution in NMP. An ink was created by the addition of more NMP (ca. 2 mL); this ink was ball-milled at 800 rpm for 1 hour and then cast onto copper foil (9 μm thickness, PI-KEM, Staffordshire, UK). The sheets were dried for 10 minutes at ca. 200 °C on a hotplate until they were superficially dry. The electrode sheets were then left to dry overnight at room temperature. After the electrodes were cut out, they were dried overnight under vacuum at 120 °C in the heated antechamber of a glovebox (MB-Unilab Plus SP, M. Braun Inertgas-Systeme, Garching, Germany). The Ar-filled glovebox (H_2O and O_2 < 1 ppm) was used for cell assembly. The active mass loading of the electrodes was in the range 1.2 to 2.0 mg cm^{-2} and their thickness was ca. 35 μm.

Li-ion half-cells in CR2032 coin cell cases were made using each of the metal germanate negative electrodes, with lithium metal discs (PI-KEM, Staffordshire, UK) as reference and counter electrodes, and Whatman GF/D glass microfiber (Buckinghamshire, UK) separators. The separators were drenched in an organic electrolyte containing 1 M $LiPF_6$ (dissolved in 1:1 volume ratio ethylenecarbonate/ethylmethylcarbonate, BASF, Ludwigshafen, Germany).

Galvanostatic and potentiodynamic cycling was carried out using an Arbin Instruments Model BT-2000 battery tester (Caltest Instruments Ltd, Guildford, UK) at room temperature in the potential range 0.05 to 3.0 V vs. Li/Li^+. The galvanostatic charge/discharge cycling was carried out at specific currents in the range 0.1 to 10.0 A g^{-1} and long-term cycling was carried out at a specific current of 0.1 A g^{-1}. Cyclic voltammetry (CV) was used for potentiodynamic measurements at scan rates in the range 0.05 to 100 mV s^{-1}. Electrochemical impedance spectroscopy (EIS) was performed for as-made Li-ion half-cells and for half-cells after 30 cycles of galvanostatic cycling. EIS was carried out on an Interface 1000 Gamry potentiostat (Gamry Instruments, Pennsylvania, US) in the range of frequencies 100 kHz to 10 mHz, using an AC voltage of 0.01 V rms.

Results & Discussion

Physical Characterisation

The as-prepared nano-powders were recovered as white, black, and light grey powders for Zn_2GeO_4, Co_2GeO_4, and Mn_2GeO_4, respectively. The powder X-ray diffraction (PXRD) patterns subsequent Rietveld refinement of the three samples revealed a different crystal

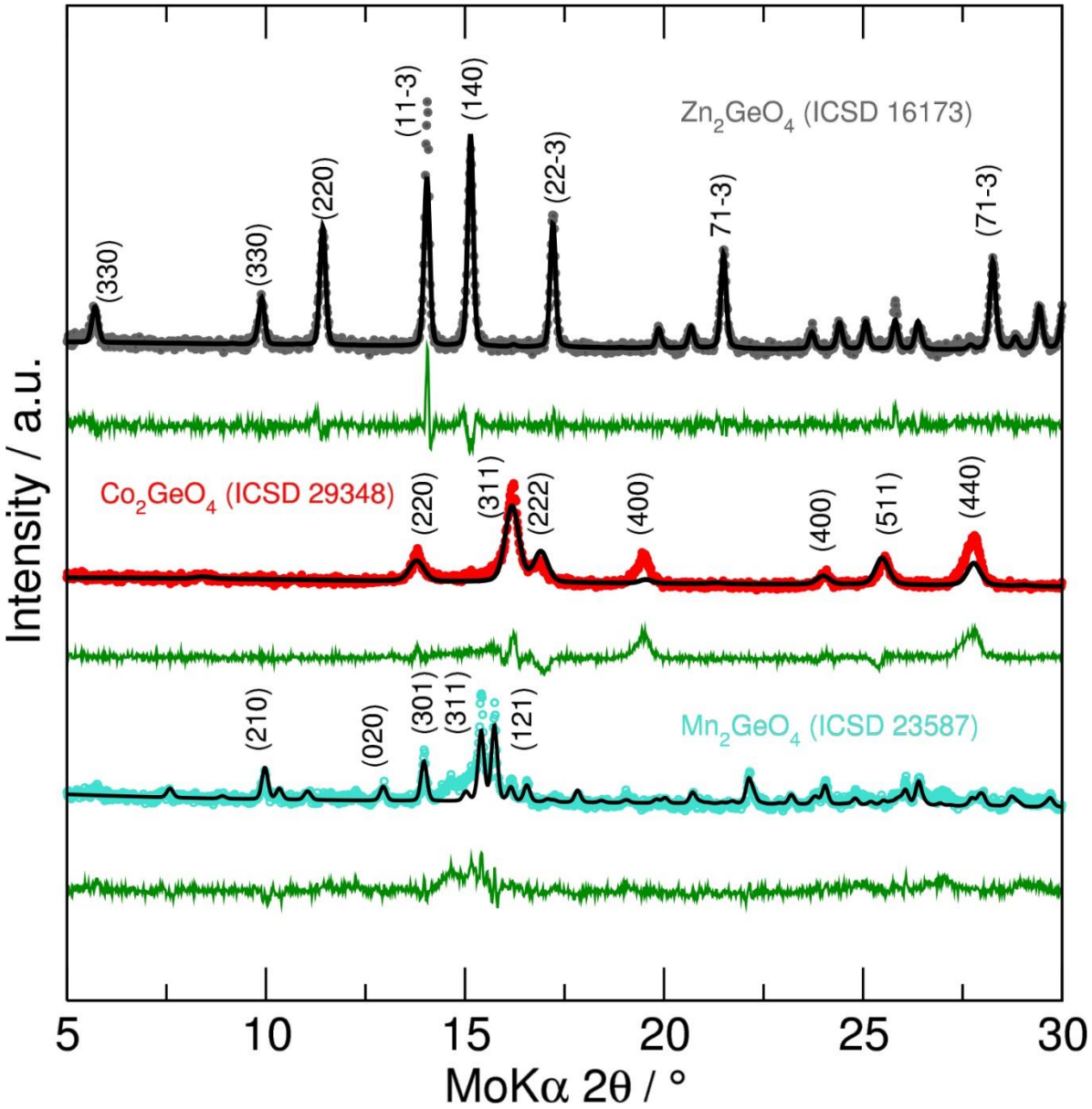

Figure 1: Powder X-ray diffraction patterns and Rietveld refinement of rhombohedral Zn_2GeO_4 (ICSD no.: 16173), spinel Co_2GeO_4 (ICSD no.: 29348) and orthorhombic Mn_2GeO_4 (ICSD no.: 23587) prepared by a continuous hydrothermal route. Calculated fits are shown as black lines with the respective residuals below each fit in green.

structure for each, as expected (see Figure 1, polyhedral models of the three structures are given in Figure S2). The pattern for Zn_2GeO_4 was a good match to the reference pattern for rhombohedral Zn_2GeO_4 (ICSD no. 16173; space group: *R*−3*H*). The major peaks corresponded to the (220), (11−3), (140), and (22−3) planes for rhombohedral Zn_2GeO_4 at 2θ = 11.7, 14.2, 15.3, and 17.2°, respectively.[24,26] The pattern for Co_2GeO_4 was a good match for the reference pattern for cubic spinel Co_2GeO_4 (ICSD no.: 29348; space group: *Fd*−3*mS*). The major peaks corresponded to (311), (400), and (440) planes for cubic spinel Co_2GeO_4 at 2θ = 16.4, 19.7, and 27.7°, respectively.[35] Significant peak broadening was also observed for Co_2GeO_4, suggesting a small crystallite domain size for the material. The PXRD pattern for Mn_2GeO_4 showed the sharpest peaks and was a good match for orthorhombic Mn_2GeO_4 (ICSD no.: 23587; space group: *Pnma*). The major peaks corresponded to the (301), (311), and (121) planes of orthorhombic Mn_2GeO_4 at 2θ = 14.2, 15.6, and 15.9°, respectively.

Equation 3 (Scherrer equation) was used to estimate the domain size of the synthesised particles:

$$d = \frac{K \times \lambda}{\beta \times \cos\theta} \qquad \text{(Eq. 3)}$$

For the Scherrer equation, *d* is crystallite size in nm, λ is the radiation source's wavelength (here Mo radiation, 0.7107 Å), β the full width at half-maximum (FWHM) of the peaks and theta the Bragg angle. The shape factor *k* can range from 0.86 to 0.98, and if unknown, was approximated to 0.9.[36] The estimated domain sizes were 24 (± 3), 11 (± 2), and 34 (± 3) nm for Zn_2GeO_4, Co_2GeO_4, and Mn_2GeO_4, respectively, which confirmed the broad conclusions drawn from the peak shapes of the PXRD patterns.

Rietveld refinement highlighted several discrepancies in the peak intensities for the three materials. These reflections were found to be (11−3) for Zn_2GeO_4, (400) and (440) for

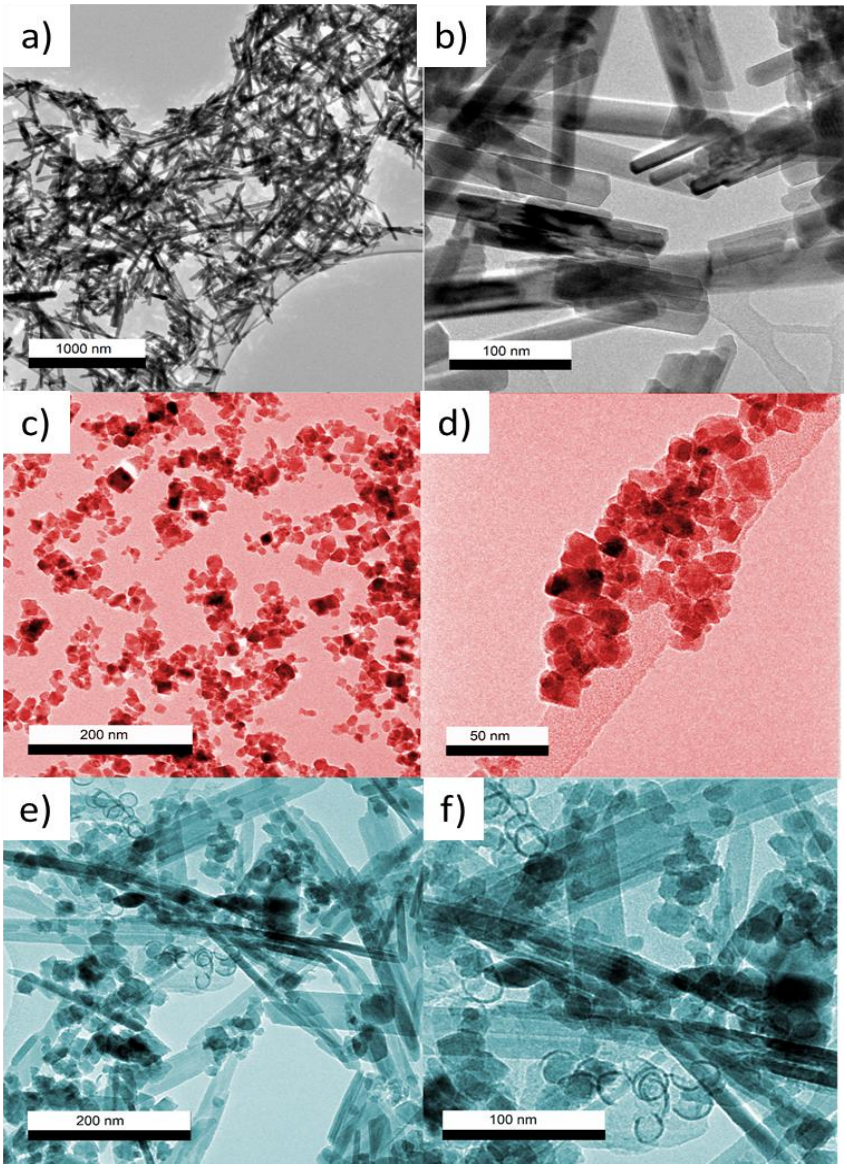

Figure 2: Transmission electron micrographs of a+b) Zn_2GeO_4 nanorods, c+d) Co_2GeO_4 nanoparticles, and e+f) Mn_2GeO_4 mixed nanoparticles/nanotubes.

Co_2GeO_4 and (311) and (121) for Mn_2GeO_4 and are likely due to preferential crystal growth in particular directions. Mn_2GeO_4 also showed a broad hump below the (311) and (121) reflections likely due to the presence of an unidentified secondary phase with low crystallinity which contributes to the lower calculated (and higher observed) reflection intensities in this material.

To investigate the potential preferential growth and size of the three germinates, transmission electron micrographs (TEM) was employed and revealed different morphologies and particle sizes for the different samples. Zn_2GeO_4 presented as nanorods, with lengths varied

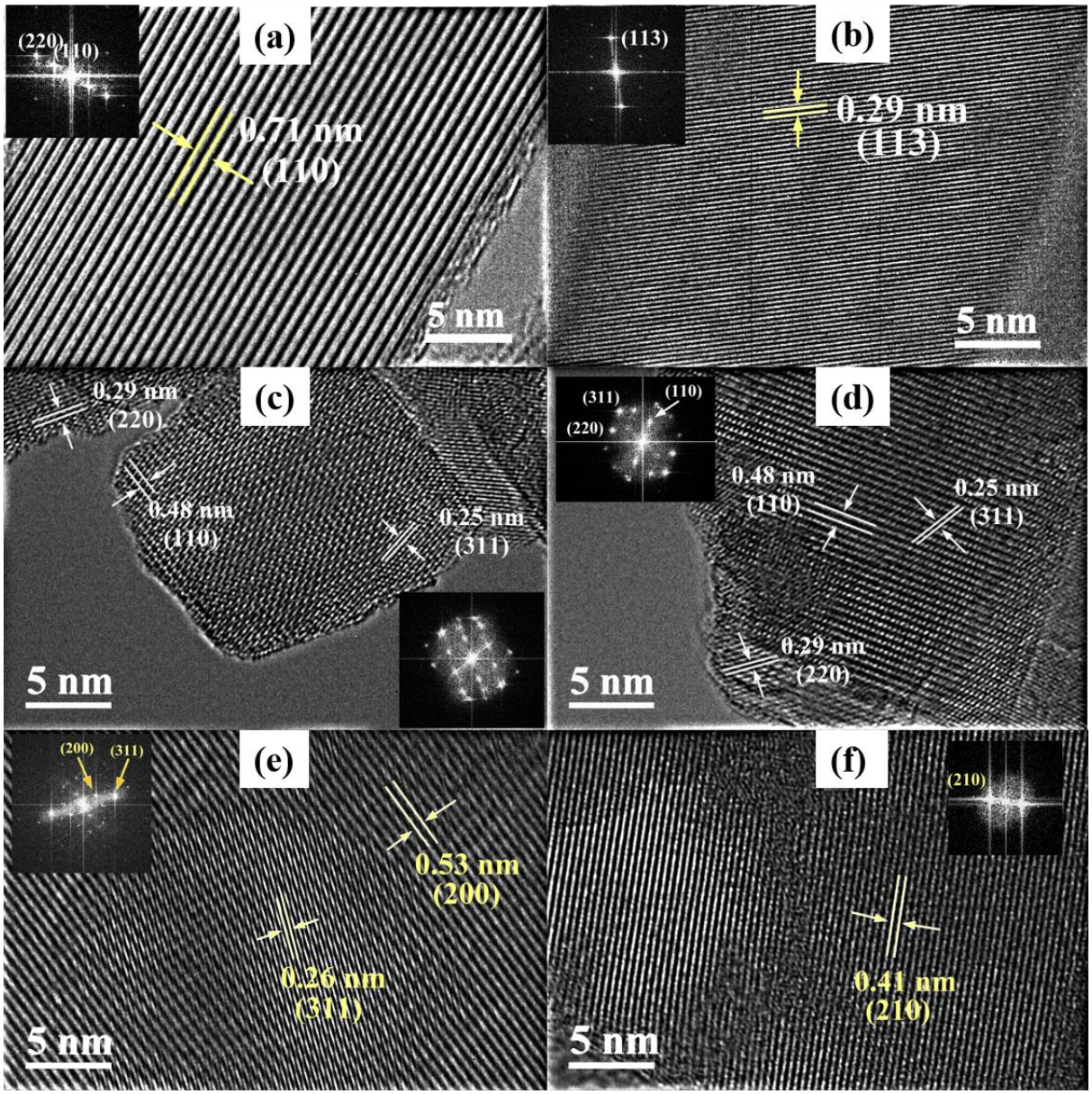

Figure 3: Hi-Resolution Transmission Electron Micrographs of (a+b) Zn_2GeO_4; (c+d) Co_2GeO_4, and (e+f) Mn_2GeO_4 nanostructures.

in the range of 50 to 500 nm and widths in the range of 10 to 20 nm, with aspect ratios ranging from 1:5 to 1:30. Co_2GeO_4 nanoparticles showed an average particle size of 17 ± 5 nm with a variety of morphologies, although most particles were spherical or cubic. Mn_2GeO_4 particles were both cube-like nanoparticles and nanotubular in structure. The nanoparticles have an average diameter of 28 ± 9 nm, while the nanotube length varied from 70 to 400 nm and widths from 10 to 60 nm. To further our understanding on the crystal structure, HRTEM was carried out on these materials. For Zn_2GeO_4, as shown in Figure 3a and b, the lattice spacings were found

to be 0.71 and 0.29 nm, corresponding to (110) and (113) lattice planes, respectively. It can also be seen that the (110) plane is oriented parallel to the nanorod (growth direction) while the (113) plane is at an angle of 66° to the growth direction of the rod. Therefore it can be stated that the hydrothermal flow synthesis resulted in Zn_2GeO_4 nanorods growing along the *c*-axis of the rhombohedral phenacite-type structure.[37,38] These Zn_2GeO_4 nanorods were single crystalline in nature with no defects. Lattice fringes for Co_2GeO_4 were found to be rather non-uniform. For Co_2GeO_4, three different overlapped lattices could be observed in Figure 3c and d. The measured *d* spacing of 0.48, 0.29 and 0.25 nm can be related to the (110), (220) and (311) planes of fcc Co_2GeO_4 structure.[39] In the case of orthorhombic Mn_2GeO_4, with unit cell dimensions a = 10.7 Å, b = 6.26 Å and c = 5.04 Å, lattice spacing for the observed peaks in the XRD pattern could calculated to be d_{210} = 0.41 nm, d_{020} = 0.30 nm , d_{301} = 0.29 nm, d_{311} = 0.26 nm , d_{121} = 0.26 nm , d_{200} = 0.53 nm. From these calculated values the observed lattice spacing of 0.26, 0.53 and 0.41 nm in Figure 3e and f can be related to the (311), (200), and (210) planes. It can be assumed that the lattices d_{311} and d_{121} have the same lattice spacing. However, by comparing the intersection angle between the lattice planes (200), (311), and (200), (121) lattices have been identified in Figure 3e. To the best of the authors' knowledge, there are no previous reports on HRTEM for Mn_2GeO_4.

Energy dispersive X-ray spectroscopy (EDX) mapping showed even distributions of the respective metal and Ge across all particles (see Figure S3). This suggested that there was no enrichment of any metal ions anywhere in or on the particles and that the materials were phase-pure. A quantitative analysis of the atomic quantities in Zn_2GeO_4, showed a concentration of 35 (±3) and 65 (±3) at% for Ge and Zn, respectively. In comparison, for Co_2GeO_4 and Mn_2GeO_4, the metal and Ge were in the at% ratios of 31(±6):69(±5) and 31(±3):69(±3), respectively. These values were in line with expectations for the as-synthesised materials.

X-ray photoelectron spectroscopy (XPS) was used to determine the oxidation states and semi-quantitative atomic concentrations on the surface of the different metal germanate particles. The Zn *2p* level binding energies showed two peaks at 1022.2 and 1045.3 eV, which were assigned to Zn $2p_{3/2}$ and Zn $2p_{1/2}$, respectively (see Figure S4a). This was in good agreement with an oxidation state of Zn(II).[40] For Co *2p* binding energies, the high-resolution spectrum showed two main peaks centred at 780.9 and 796.9 eV, corresponding to Co $2p_{3/2}$ and Co $2p_{1/2}$, respectively. The two satellite peaks at 785.7 and 802.9 eV (see Figure S4b) are identifiers for Co(II) and, therefore, confirmed the expected oxidation state of Co as +2 valence.[35] For the high-resolution Mn *2p* spectrum, the Mn $2p_{3/2}$ and Mn $2p_{1/2}$ peaks were centred at 641.5 and 653.3 eV, respectively (see Figure S4c). The shake-up satellite feature between the two peaks is only associated with the Mn(II) oxidation state of Mn; hence, this confirmed the expected oxidation state of Mn as +2.[41] For the Ge *3d* spectra of the three samples, the single intense peak of Ge *3d* centred at 32.3, 32.3, and 32.4 eV for Zn_2GeO_4, Co_2GeO_4, and Mn_2GeO_4, respectively (see Figure S4d), was in the location usually associated with germania and, therefore, an oxidation state of Ge(IV).[35,40] Semi-quantitative analysis of the peak areas of the spectra from XPS showed M:Ge at% ratios of 70:30 (M=Zn), 67:33 (M = Co), and 64:36 (M = Mn).

The Brunauer-Emmett-Teller (BET) N_2 absorption/desorption measurements revealed significant differences in specific surface areas (SSA) for the three samples (see Figure S5). The SSAs were 28, 65, and 44 $m^2\ g^{-1}$ for Zn_2GeO_4, Co_2GeO_4, and Mn_2GeO_4, respectively. Therefore, Co_2GeO_4 showed the highest SSA, the smallest estimated domain size, and the smallest particles according to the electron micrographs. Mn_2GeO_4 showed the second largest SSA, but the largest estimated domain size, however, this could have been a result of the two different morphologies of Mn_2GeO_4 as observed from TEM. Finally, Zn_2GeO_4 showed the

largest particles in the micrographs due to the rod-like morphology and the smallest SSA; the relatively high estimated domain size aligned well with this.

Electrochemical Characterization

To explore the lithiation and delithiation mechanisms for the half cells, potentiodynamic cyclic voltammetries and galvanostatic charge/discharge cycling were carried out in the potential window 3.00 to 0.05 V vs. Li/Li^+. The cyclic voltammograms (CVs) for the first three cycles were plotted in Figure 4. In the first cathodic sweep for the cell containing Zn_2GeO_4, a sharp peak at 0.7 V vs. Li/Li^+ corresponded to a combination of the reduction/decomposition of Zn_2GeO_4, the formation of solid electrolyte interphase (SEI), and the formation of Li_xZn alloy (see Figure 4a). At potentials below 0.3 V vs. Li/Li^+, another peak arose as the result of the formation of Li_xGe alloy.[42,43] Upon delithiation, two peaks appeared, centred at ca. 0.5 and 1.1 V vs. Li/Li^+. They were previously been assigned to the delithiation of the Li_xGe alloy and the combined delithiation of the Li_xZn as well as the partial oxidation of Zn and Ge, respectively.[42,43] This means that the lithiation and delithiation mechanism could be broadly expected to be as follows (see Equations 4 to 8);

$$Zn_2GeO_4 + 8Li^+ + 8e^- \rightarrow 2Zn + Ge + 4Li_2O \quad \text{(First lithiation, irreversible: Eq. 4)}$$

$$Ge + xLi^+ + xe^- \leftrightarrow Li_xGe\ (x \leq 4.4) \quad \text{(Lithiation/delithiation, reversible: Eq. 5)}$$

$$Zn + xLi^+ + xe^- \leftrightarrow Li_xZn\ (x \leq 1.0) \quad \text{(Lithiation/delithiation, reversible: Eq. 6)}$$

$$Zn + Li_2O \leftrightarrow ZnO + 2Li^+ + 2e^- \quad \text{(Lithiation/delithiation, reversible: Eq. 7)}$$

$$Ge + 2Li_2O \leftrightarrow GeO_2 + 4Li^+ + 4e^- \quad \text{(Lithiation/delithiation, reversible: Eq. 8)}$$

The reversibility of the process could be seen in the similarity of the plots for the second and third cycles. There was a significant shift in peak position for the first cathodic peak in the

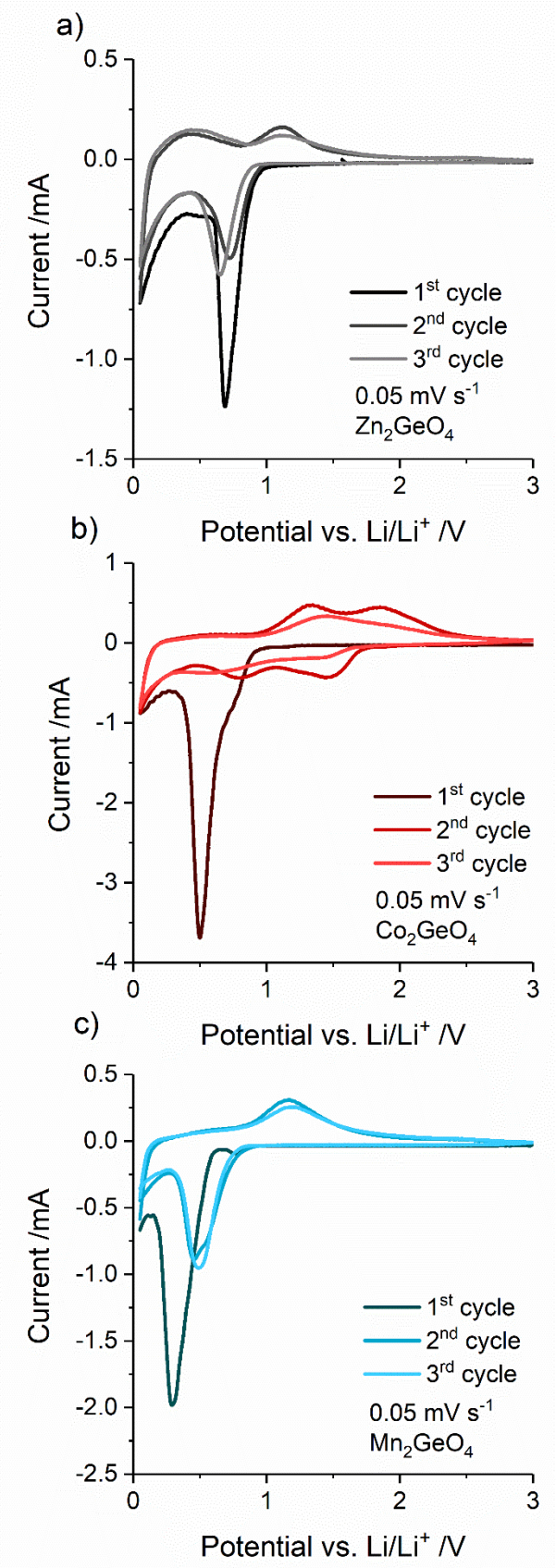

Figure 5: First three cycles of the cyclic voltammetries at a scan rate of 0.05 mV s^{-1} for a) Zn_2GeO_4, b) Co_2GeO_4, and c) Mn_2GeO_4.

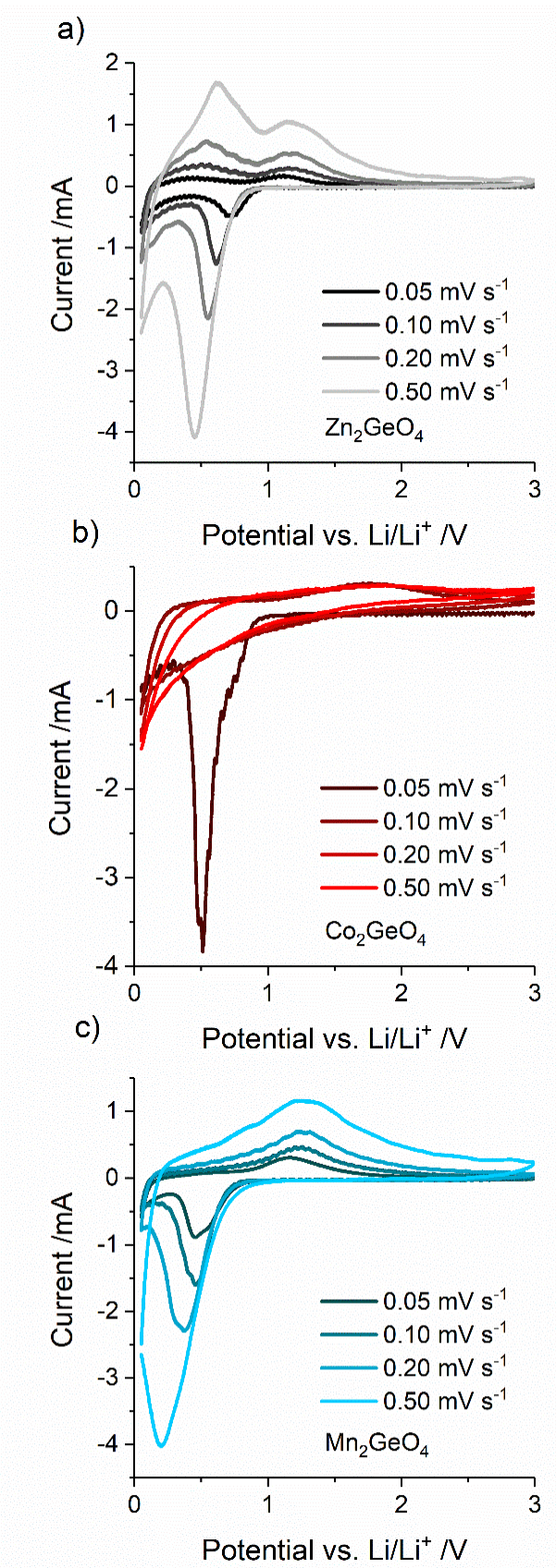

Figure 5: Cyclic voltammetries at the range of scan rates 0.05 to 0.50 mV s^{-1} for a) Zn_2GeO_4, b) Co_2GeO_4, and c) Mn_2GeO_4.

second cycle compared to the first cycle, which indicated the different lithiation process

occurring (GeO_2 and ZnO reduction instead of Zn_2GeO_4 decomposition).

The CV for the first cycle of the cell containing Co_2GeO_4 revealed a major peak at ca. 0.6 V vs. Li/Li^+ during the first lithiation, which has previously been associated with the decomposition of Co_2GeO_4, the formation of an SEI layer, and the alloying reaction of Li_xGe.[20] Upon delithiation, two peaks appeared in the CV at ca. 1.2 and 2.0 V vs. Li/Li^+ (see Figure 4b). The peak at lower potential was assigned as the delithiation and re-oxidation of Ge, whereas the peak at higher potential was associated with re-oxidation of Co to CoO. However, the reversibility for this process was not as substantive as that for the cell containing Zn_2GeO_4. During the second lithiation of the cell containing Co_2GeO_4, there were peaks at ca. 1.5 and 0.9 V vs. Li/Li^+, which is in agreement with previous reports in the literature.[20] The whole lithiation and delithiation process for the cobalt germanate could, therefore, be described as follows;

$$Co_2GeO_4 + 8Li^+ + 8e^- \rightarrow 2Co + Ge + 4Li_2O$$ (First lithiation, irreversible: Eq. 9)

$$Ge + xLi^+ + xe^- \leftrightarrow Li_xGe\ (x \leq 4.4)$$ (Lithiation/delithiation, reversible: Eq. 10)

$$Co + Li_2O \leftrightarrow CoO + 2Li^+ + 2e^-$$ (Lithiation/delithiation, reversible: Eq. 11)

$$Ge + 2Li_2O \leftrightarrow GeO_2 + 4Li^+ + 4e^-$$ (Lithiation/delithiation, reversible: Eq. 12)

For the cell containing Mn_2GeO_4, the first lithiation (cathodic sweep) showed a very small and a very large peak at ca. 0.7 and 0.3 V vs. Li/Li^+, respectively. The small peak was assigned to the formation of a SEI layer,[11,23] whereas the major peak was ascribed to the decomposition of Mn_2GeO_4 and the alloying of Li_xGe. Interestingly, the decomposition of Mn_2GeO_4 occurred at significantly lower potentials vs. Li/Li^+ than for M_2GeO_4 (M = Co or Zn). Upon delithiation, there was a single peak at ca. 1.2 V vs. Li/Li^+, which could be associated with the re-oxidation of Ge[11,23], however, the same potential has previously also been assigned

as the re-oxidation of Mn to MnO.[44] Upon the second lithiation, the single peak shifted to ca. 0.5 V vs. Li/Li^+, similar to the potential reported for the cathodic peak in the second cycle for Zn_2GeO_4. This suggested that in this case, the peak could be associated with the reduction of both GeO_2 and MnO as well as the alloying reaction for Li_xGe. Thereafter, peak shapes and sizes remained similar, indicating good reversibility. The whole lithiation and delithiation process could therefore be described as follows;

$$Mn_2GeO_4 + 8Li^+ + 8e^- \rightarrow 2Co + Ge + 4Li_2O$$ (First lithiation, irreversible: Eq. 13)

$$Ge + xLi^+ + xe^- \leftrightarrow Li_xGe\ (x \leq 4.4)$$ (Lithiation/delithiation, reversible: Eq. 14)

$$Mn + Li_2O \leftrightarrow CoO + 2Li^+ + 2e^-$$ (Lithiation/delithiation, reversible: Eq. 15)

$$Ge + 2Li_2O \leftrightarrow GeO_2 + 4Li^+ + 4e^-$$ (Lithiation/delithiation, reversible: Eq. 16)

To further elucidate the potentiodynamic properties of the different metal germanates, the Li-ion half-cells were cycled in the range of scan rates 0.05 to 10.0 mV s^{-1}. Except for a shift in the peak positions due to higher overpotentials, the shapes of the CVs for Zn_2GeO_4 remained constant, indicating good rate properties (see Figure 5a). At a scan rate of 0.50 mV s^{-1}, the lithiation peak had shifted to ca. 0.50 V vs. Li/Li^+, whereas the delithiation peaks had shifted to ca. 0.55 and 1.10 V vs. Li/Li^+.

The scan rate tests for the half-cell with Co_2GeO_4 revealed poor rate performance; the peaks for Co and Ge re-oxidation disappeared almost completely at a scan rate of 0.50 mV s^{-1} (see Figure 5b). The CVs for the cell containing Mn_2GeO_4 at different scan rates revealed excellent rate performance and significant peak broadening (see Figure 5c). The good rate performance of M_2GeO_4 (M = Zn or Mn) compared to Co_2GeO_4 resulted in higher specific capacities at higher scan rates (see Figure S6). For example, at a scan rate of 1.0 mV s^{-1}, the specific capacities were ca. 480, 50, and 305 mAh g^{-1} for M_2GeO_4 (M = Zn, Co and Mn,

respectively). Whilst the CVs for M_2GeO_4 (M = Zn or Mn) showed significant peaks even at a scan rate of 10.0 mV s^{-1}, the CV for Co_2GeO_4 showed barely any charge storage (see Figure S7).

The charge storage properties of the three metal germanate containing half-cells were further investigated using galvanostatic charge/discharge cycling (see Figure 6). All the cells showed a similar specific delithiation capacity in the first cycle. They were ca. 650, 660, and 725 mAh g^{-1} for the cells containing M_2GeO_4, (M = Zn, Co, Mn), respectively, at a specific current of 0.1 A g^{-1}. For all cells, Coulombic efficiencies for the first cycle were < 60 % due to first cycle losses from the irreversible decomposition of the initial M_2GeO_4 compounds, the formation of an SEI, and other irreversible processes. Whilst the cells containing Zn_2GeO_4 and Mn_2GeO_4 showed stable cycling (specific capacities falling to ca. 600 and 510 mAh g^{-1},

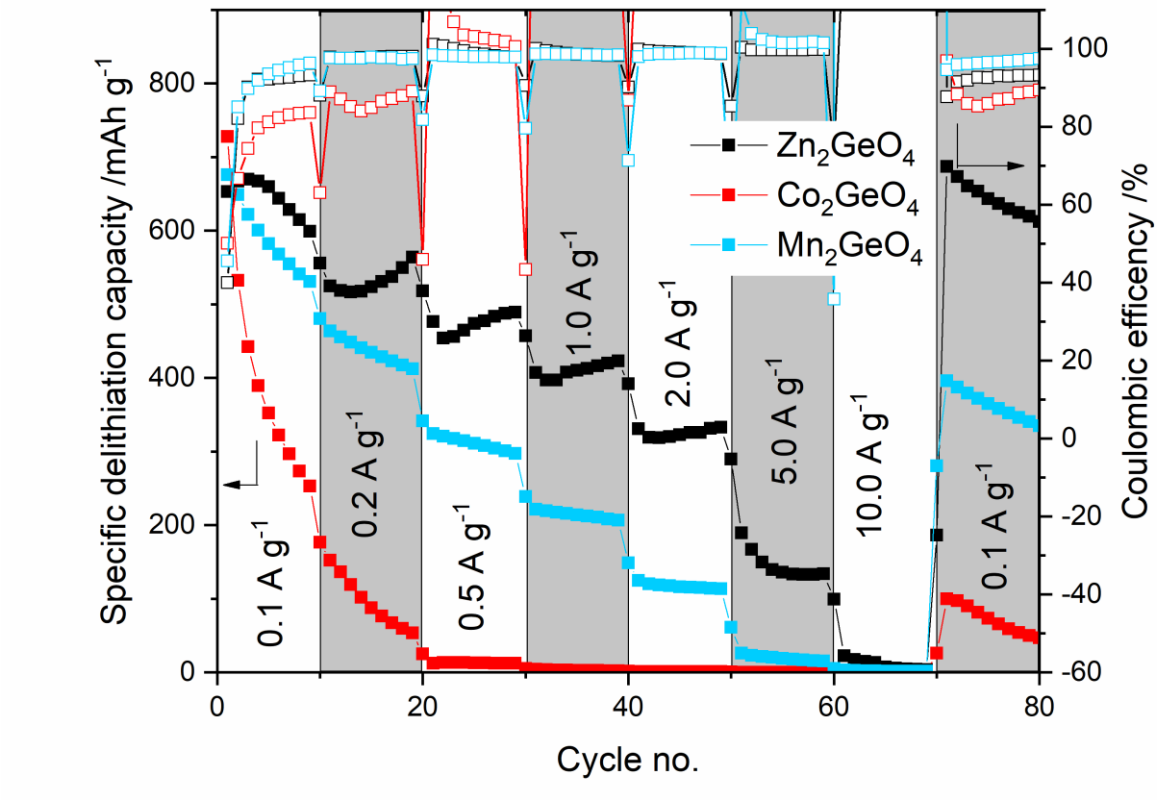

Figure 6: Specific delithiation (charge) capacities of the galvanostatic C-rate tests for the three germanates (left axis) along with the corresponding Coulombic efficiencies (right axis).

respectively for 10 cycles at 0.1 A g^{-1}), the specific capacity of the cell containing Co_2GeO_4 fell to ca. 240 mAh g^{-1}. The same cell for Co_2GeO_4 also showed significantly poorer rate performance than the other samples. Furthermore, whilst the cell containing Co_2GeO_4 did not store any charge at a specific current of 1.0 A g^{-1}, cells containing M_2GeO_4 (M = Zn and Mn) still showed specific capacities of ca. 420 and 220 mAh g^{-1}, respectively. Even at a specific capacity of 2.0 A g^{-1}, the cells with M_2GeO_4 (M = Zn and Mn) showed specific capacities of 350 and 130 mAh g^{-1}, respectively. After cycling cells at different current rates up to 10 A g^{-1}, the current rate was returned to 0.1 A g^{-1}, yielding specific capacities of 660, 380, and 80 mAh g^{-1} for the cells containing the metal germinates M_2GeO_4, (where M= Zn, Mn and Co), respectively.

The first three cycles of galvanostatic charge/discharge cycling at a specific current of 0.1 A g^{-1} were plotted in **Error! Reference source not found.**. For the cell containing Zn_2GeO_4, in the first cycle, the lithiation confirmed the process as described for the CVs above (see **Error! Reference source not found.**a); a plateau at ca. 0.9 V vs. Li/Li^+ indicated the decomposition of Zn_2GeO_4, whereas the additional capacity in the sloped part of the curve at potentials below 0.9 V vs. Li/Li^+ incorporated the alloying of Zn and Ge with Li. During the delithiation, there were two distinct slopes, the one at lower potentials vs. Li/Li^+ caused by the delithiation of Li_xGe and the one at higher potentials vs. Li/Li^+ caused by the delithiation of Li_xZn and the re-oxidation of Ge and Zn. The second and third lithiation and delithiation curves were nearly identical, indicating excellent reversibility.For the cell containing Co_2GeO_4, the lithiation in the first cycle showed a region with a gentle slope in the range of potentials 0.9 to 0.6 V vs. Li/Li^+, which could be ascribed to the decomposition of Co_2GeO_4. However, the comparison between the first three cycles and the capacity fade during these cycles showed the poor reversibility of the lithiation and delithiation. For the cell containing Mn_2GeO_4, the first lithiation showed a plateau at ca. 0.5 V vs. Li/Li^+, which could be ascribed to the decomposition

of Mn_2GeO_4. The decomposition of Mn_2GeO_4 occurred at lower potentials than those of M_2GeO_4 (M = Zn or Co), as previously observed from the potentiodynamic measurements. Upon subsequent delithiation, a region with a gentle slope in the region 1.0 to 1.4 V vs. Li/Li^+ suggested the re-oxidation of Mn and Ge, whereas the region below 1.0 V vs. Li/Li^+, (with a steeper slope), could be ascribed to the delithiation of Li_xGe. The reversibility of the lithiation and delithiation reactions of Mn_2GeO_4 were confirmed by the small differences between the charge/discharge curves of different cycles.

An analysis of the galvanostatic charge/discharge curves at varying specific currents was conducted (see Figure 8). The charge/discharge curves for the fifth cycle at 0.1 A g^{-1} and for the fifth cycle after returning the specific current to 0.1 A g^{-1} after testing at different specific currents (dashed line) were nearly identical for Zn_2GeO_4 (see Figure 8a), indicating excellent reversibility. The cyclability of the cell

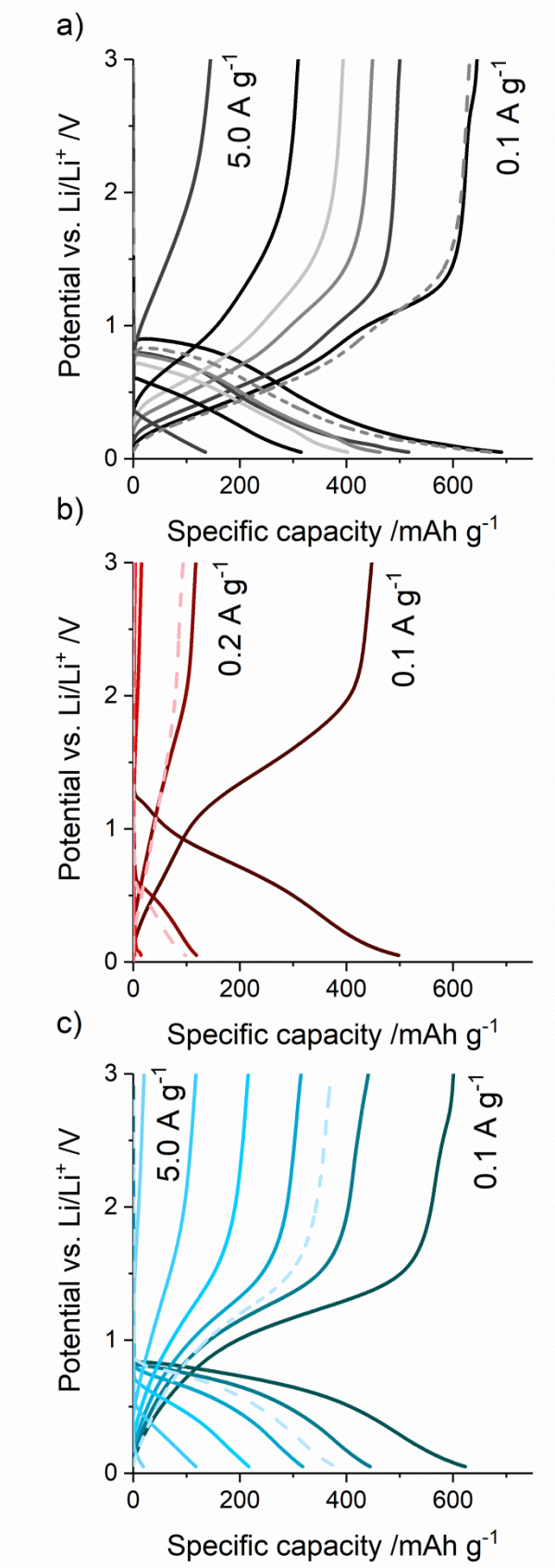

Figure 7: Charge/discharge curves at varying specific currents (0.1–5.0 A g^{-1}) for a) Zn_2GeO_4, b) Co_2GeO_4, and c) Mn_2GeO_4.

containing Co_2GeO_4 was much poorer (see Figure 8b), whereas that for the cell containing Mn_2GeO_4 (see Figure 8c) was intermediate. At higher specific currents, the shape of the curves did not significantly differ for Zn_2GeO_4 in the specific current range 0.1 to 1.0 A g^{-1}. Even at 1.0 A g^{-1}, the delithiation curve still showed evidence of the two contributors to specific capacity. For Co_2GeO_4, on the other hand, the gentle slope in the range 1.0 to 2.0 V vs. Li/Li^+ during the discharge at 0.1 A g^{-1} disappeared almost completely even at 0.2 A g^{-1}. For Mn_2GeO_4, the contribution factors to the delithiation capacity were still observable even at 1.0 A g^{-1}, although the specific capacity had fallen to ca. 190 mAh g^{-1}.

To further analyse the cycling stability of the different samples, half-cells were cycled at a specific current of 0.1 A g^{-1} for 60 cycles (see Figure 9). The cell containing Zn_2GeO_4 showed superior cycling stability compared to the others. The specific capacity of Zn_2GeO_4

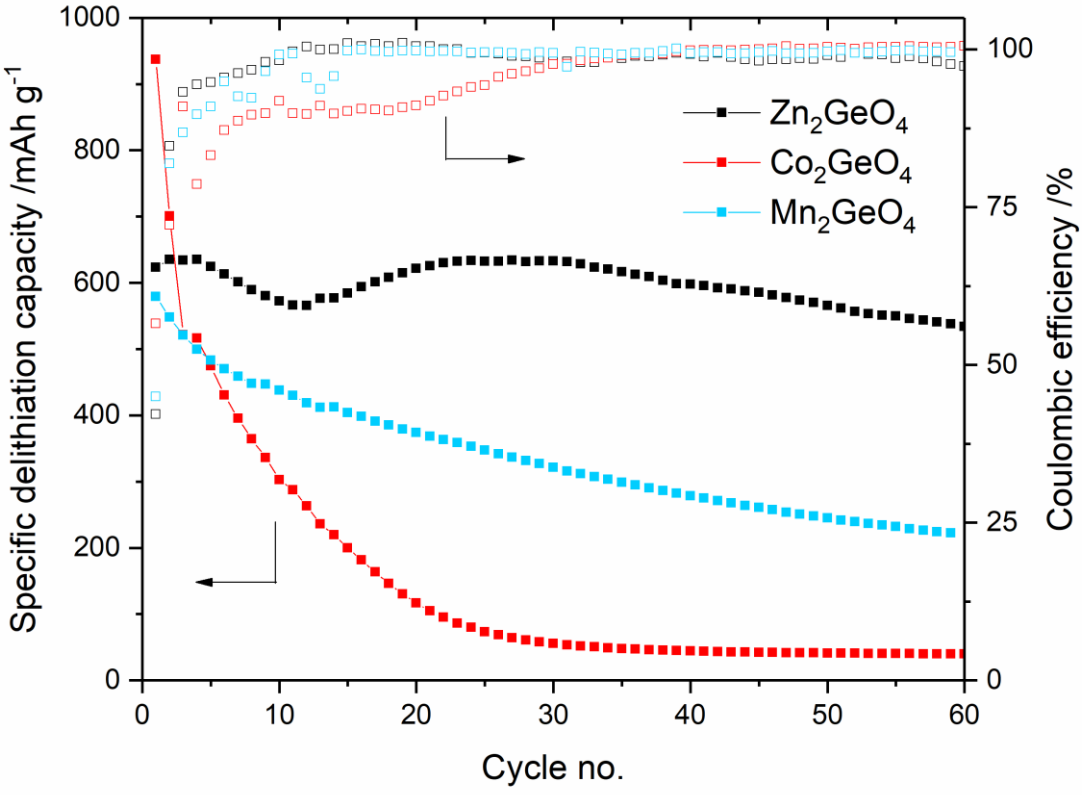

Figure 8: Long term galvanostatic cycling for the three metal germanates at a specific current of 0.1 A g^{-1}.

fell from 625 mAh g^{-1} in the first cycle to 540 mAh g^{-1} after 60 cycles, indicating a capacity retention of ca. 87 %. For cells containing M_2GeO_4 (M = Co or Mn), the initial specific capacities were 935 and 580 mAh g^{-1}, respectively. After 60 cycles, these fell to 40 and 225 mAh g^{-1}, respectively, indicating capacity losses of ca. 95 and 61 %, respectively. Alloying materials reported in the literature often suffer from poor reversibility and rate performance. For example, a comparison of ball-milled and commercial nanoparticular Si as negative electrode materials showed that the specific discharge capacities fell from ca. 2700 and 2600 mAh g^{-1} for ball-milled and commercial Si to ca. 850 and 500 mAh g^{-1}, respectively, after 20 cycles (at a rate of C/20).[45] Attempts to improve the performance of alloying materials often require more complicated syntheses and the introduction of additional active phases. For example, Si/TiO_2 composites have been explored and showed improved capacity retention. Nevertheless, the capacity retention after 50 cycles was still only 14, 23, and 34 % for Si:TiO_2 molar ratios of 1:1, 1:2, and 1:4, respectively.[46] Si wrapped in V_2O_5 nanosheets has been explored, but even for these the specific capacity fell from ca. 900 to 550 mAh g^{-1} over 20 cycles at a specific capacity of 0.5 A g^{-1} (after having been cycled at varying specific currents for 30 cycles).[47]

Furthermore, electrochemical impedance spectroscopy (EIS) was conducted, both for freshly made half-cells and for half-cells that had been cycled galvanostatically for 30 cycles at a specific current of 0.1 A g^{-1}. Before cycling, M_2GeO_4 (M = Co or Mn) appeared to have similarly low charge transfer resistance (see Figure S8a), whereas the charge transfer resistance of the cell containing Zn_2GeO_4 was slightly higher. After cycling, the charge transfer resistance increased for all samples. However, whilst the increase in charge transfer resistances seemed fairly limited for Zn_2GeO_4 and Mn_2GeO_4 (which showed very similar charge transfer resistances after cycling), the increase for Co_2GeO_4 was significantly larger. This might explain the poor cycling stability as well as the poor rate properties of the material.

Conclusions

Nanosized metal germanates (M_2GeO_4; M = Co, Mn, Zn) samples were successfully synthesised via a continuous hydrothermal flow synthesis method for the first time. The products showed a diverse range of morphologies and crystal structures. Phase pure rhombohedral Zn_2GeO_4 nanorods, cubic spinel Co_2GeO_4 nanoparticles, and orthorhombic Mn_2GeO_4 nanotubes/nanoparticles were synthesised. The samples were analysed electrochemically as negative electrodes for Li-ion half-cells and the different reaction mechanisms described and contrasted. Zn2GeO4 showed excellent performance, due to its morphology and the alloying and conversion mechanisms of both Zn and Ge. After 10 and 60 cycles (at a specific current of 0.1 A g^{-1}), Zn_2GeO_4 showed a specific capacity of 600 and 540 mAh g^{-1}, respectively, in excess of the maximum theoretical capacity of commercial graphite anodes (372 mAh g^{-1}). At higher specific currents, e.g. 2.0 A g^{-1}, Zn_2GeO_4 still retained a specific capacity of 350 mAh g^{-1}, indicating excellent rate properties.

For the first time, Mn_2GeO_4 was studied as a potential active material for Li-ion battery negative electrodes. It showed good performance at a specific current of 0.1 A g^{-1}, with a specific capacity of 510 mAh g^{-1} after 10 cycles. Mn_2GeO_4 also showed good rate performance, with a specific capacity of 220 mAh g^{-1} at a specific current of 1.0 A g^{-1}. The good electrochemical properties were argued to be a result of both the alloying and conversion reactions of Ge and the conversion reaction of Mn. Therefore, it has been shown that continuous hydrothermal synthesis presents an excellent method for the scalable synthesis of nanosized germanates. Furthermore, we have shown that some of these germanates are promising materials for negative electrode materials in LIBs and that whilst some germanates such as Zn_2GeO_4 have received widespread attention, others such as Mn_2GeO_4 have been underexplored and offer promise for future research.

Acknowledgements

The EPSRC are thanked for funding the Centre for Doctoral Training in Molecular Modelling and Materials Science (UCL, UK). JAIST (Kanazawa, Japan) are thanked for supporting a studentship for DB. JAD thanks EPSRC for support of the Joint University Industry Consortium for Energy materials and Devices (JUICED) hub (EP/R023662/1).

Bibliography

1 M. Armand and J.-M. Tarascon, *Nature*, 2008, **451**, 652–657.
2 M. R. Palacín, *Chem. Soc. Rev.*, 2009, **38**, 2565–2575.
3 P. G. Bruce, B. Scrosati and J.-M. Tarascon, *Angew. Chemie Int. Ed.*, 2008, **47**, 2930–2946.
4 K. Tang, X. Mu, P. a. van Aken, Y. Yu and J. Maier, *Adv. Energy Mater.*, 2013, **3**, 49–53.
5 P. V. Braun, J. Cho, J. H. Pikul, W. P. King and H. Zhang, *Curr. Opin. Solid State Mater. Sci.*, 2012, **16**, 186–198.
6 S. Goriparti, E. Miele, F. De Angelis, E. Di Fabrizio, R. Proietti Zaccaria and C. Capiglia, *J. Power Sources*, 2014, **257**, 421–443.
7 M. Ge, J. Rong, X. Fang and C. Zhou, *Nano Lett.*, 2012, **12**, 2318–2323.
8 Z.-W. Fu, F. Huang, Y. Zhang, Y. Chu and Q.-Z. Qin, *J. Electrochem. Soc.*, 2003, **150**, A714.
9 R. A. Huggins, *J. Power Sources*, 1999, **81**–**82**, 13–19.
10 W. J. Zhang, *J. Power Sources*, 2011, **196**, 877–885.
11 Y. Feng, X. Li, Z. Shao and H. Wang, *J. Mater. Chem. A*, 2015, **3**, 15274–15279.
12 S. Yuvaraj, R. K. Selvan and Y. S. Lee, *RSC Adv.*, 2016, **6**, 21448–21474.
13 N. Liu, H. Wu, M. T. McDowell, Y. Yao, C. Wang and Y. Cui, *Nano Lett.*, 2012, **12**, 3315–3321.
14 J. Cabana, L. Monconduit, D. Larcher and M. R. Palacín, *Adv. Mater.*, 2010, **22**, E170–E192.
15 L. Croguennec and M. R. Palacin, *J. Am. Chem. Soc.*, 2015, **137**, 3140–3156.
16 Y. M. Lin, K. C. Klavetter, A. Heller and C. B. Mullins, *J. Phys. Chem. Lett.*, 2013, **4**, 999–1004.
17 J. Graetz, C. C. Ahn, R. Yazami and B. Fultz, *J. Electrochem. Soc.*, 2004, **151**, A698.
18 T. Song, Y. Jeon, M. Samal, H. Han, H. Park, J. Ha, D. K. Yi, J. M. Choi, H. Chang, Y. M. Choi and U. Paik, *Energy Environ. Sci.*, 2012, **5**, 9028–9033.
19 W. Liang, H. Yang, F. Fan, Y. Liu, X. H. Liu, J. Y. Huang, T. Zhu and S. Zhang, *ACS Nano*, 2013, **7**, 3427–3433.
20 S. Jin, G. Yang, H. Song, H. Cui and C. Wang, *ACS Appl. Mater. Interfaces*, 2015, **7**, 24932–24943.
21 J. S. Peña, I. Sandu, O. Joubert, F. S. Pascual, C. O. Areán and T. Brousse, *Electrochem. Solid-State Lett.*, 2004, **7**, A278.
22 W. Chen, L. Lu, S. Maloney, Y. Yang and W. Wang, *Phys. Chem. Chem. Phys.*, 2015, **17**, 5109–5114.
23 F. Zou, X. Hu, L. Qie, Y. Jiang, X. Xiong, Y. Qiao and Y. Huang, *Nanoscale*, 2014, **6**,

924–930.
24 Q. Li, X. Miao, C. Wang and L. Yin, *J. Mater. Chem. A*, 2015, **3**, 21328–21336.
25 R. Wang, S. P. Wu, Y. C. Lv and Z. Q. Lin, *Langmuir*, 2014, **30**, 8215–8220.
26 J. K. Feng, M. O. Lai and L. Lu, *Electrochem. commun.*, 2011, **13**, 287–289.
27 W. Chen, S. Maloney and W. Wang, *Electrochim. Acta*, 2015, **176**, 96–102.
28 R. I. Gruar, C. J. Tighe and J. A. Darr, *Ind. Eng. Chem. Res.*, 2013, **52**, 5270–5281.
29 J. A. Darr, J. Zhang, N. M. Makwana and X. Weng, *Chem. Rev.*, 2017, **117**, 11125–11238.
30 D. Bauer, A. J. Roberts, C. L. Starkey, R. Vedarajan, D. J. L. Brett, P. R. Shearing, N. Matsumi and J. A. Darr, *Int. J. Electrochem. Sci.*, 2018, **13**, 5120–5140.
31 D. Bauer, A. J. Roberts, S. G. Patnaik, D. J. L. Brett, P. R. Shearing, E. Kendrick, N. Matsumi and J. A. Darr, *J. Electrochem. Soc.*, 2018, **165**, A1662–A1670.
32 D. Bauer, A. J. Roberts, N. Matsumi and J. A. Darr, *Nanotechnology*, 2017, **28**, 195403.
33 US2013/0136687 A1, 2013.
34 C. J. Denis, C. J. Tighe, R. I. Gruar, N. M. Makwana and J. A. Darr, *Cryst. Growth Des.*, 2015, **15**, 4256–4265.
35 S. Jin, G. Yang, H. Song, H. Cui and C. Wang, *ACS Appl. Mater. Interfaces*, 2015, **7**, 24932–24943.
36 U. Holzwarth and N. Gibson, *Nat. Nanotechnol.*, 2011, **6**, 534–534.
37 S. Yan, L. Wan, Z. Li and Z. Zou, *Chem. Commun.*, 2011, **47**, 5632.
38 S. Wu, Z. Wang, X. Ouyang and Z. Lin, *Nanoscale*, 2013, **5**, 12335–12341.
39 X. Ge, S. Song and H. Zhang, *CrystEngComm*, 2012, **14**, 7306.
40 J. Liu, G. Zhang, J. C. Yu and Y. Guo, *Dalt. Trans.*, 2013, **42**, 5092.
41 M. C. Biesinger, B. P. Payne, A. P. Grosvenor, L. W. M. Lau, A. R. Gerson and R. S. C. Smart, *Appl. Surf. Sci.*, 2011, **257**, 2717–2730.
42 Y. Chen, Y. Lin, N. Du, C. Xiao, S. Wu, Y. Zhang and D. Yang, *Energy Technol.*, 2017, **5**, 1656–1662.
43 R. Yi, J. Feng, D. Lv, M. L. Gordin, S. Chen, D. Choi and D. Wang, *Nano Energy*, 2013, **2**, 498–504.
44 J. Chen, Y. Wang, X. He, S. Xu, M. Fang, X. Zhao and Y. Shang, *Electrochim. Acta*, 2014, **142**, 152–156.
45 I. Sandu, P. Moreau, D. Guyomard, T. Brousse and L. Roué, *Solid State Ionics*, 2007, **178**, 1297–1303.
46 Y. Yang, Y. Bai, S. Zhao, Q. Chang and W. Zhang, *J. Alloys Compd.*, 2013, **579**, 7–11.
47 G. Carbonari, F. Maroni, A. Birrozzi, R. Tossici, F. Croce and F. Nobili, *Electrochim. Acta*, 2018, **281**, 676–683.